Anomalous valley Hall effect induced by sublattice symmetry breaking in ABX_3 honeycomb kagomé lattice

Bingwen Zhang [1,*] Fubao Zheng,[2] Xuejiao Chen,[3] Fenglin Deng,[3] and Jun Wang [1,†]

[1]*Fujian Key Laboratory of Functional Marine Sensing Materials, Center for Advanced Marine Materials and Smart Sensors, College of Material and Chemical Engineering, Minjiang University, Fuzhou 350108, People's Republic of China*

[2]*School of Science, Shandong Jianzhu University, Jinan 250101, People's Republic of China*

[3]*Key Laboratory of Magnetic Materials and Devices and Zhejiang Province Key Laboratory of Magnetic Materials and Application Technology, Ningbo Institute of Materials Technology and Engineering, Chinese Academy of Sciences, Ningbo 315201, People's Republic of China*

Valley polarization, the preferential occupation of electrons in certain valleys of the energy band structure, has recently emerged as a promising concept in the field of valleytronics, which aims to exploit the valley degree of freedom of electrons for information processing and storage. In two-dimensional (2D) ABX_3 (A and B represent two different metals, and X represents ligand) hexagonal kagomé (HK) lattice, we proposed a general four-band tight-binding model to explain the phase transition from quantum anomalous Hall effect to anomalous valley Hall effect by substituting one metal A with a different metal B from HK lattice A_2X_3. To confirm the result of the model, we performed density functional theory calculations to study the electronic structure of 2D HK lattice $NbV(C_6H_4)_3$, $TaNb(C_6H_4)_3$, and $TaNbO_3$, which exhibit large spontaneous valley polarization. The valley polarization emerged by effect of spin orbit coupling and the polarization could be tuned by spin direction. Our results reveal the mechanism of valley physics in ABX_3 HK lattice and shed light on future prediction of vallytronics exploration and may have potential applications in the field of valleytronics.

I. INTRODUCTION

The manipulation of the valley degree of freedom of electrons in crystalline materials has recently emerged as a promising concept in the field of valleytronics. Valleytronics is motivated by the potential for information storage and processing advantages that go beyond traditional charge- and spin-based semiconductor technologies [1–3]. Valley polarization, the preferential occupation of electrons in certain valleys of the energy band structure, is a key property that is exploited in valleytronic systems.

The potential for manipulating the valley degree of freedom in two-dimensional (2D) materials has sparked interest in developing valleytronic devices, including field-effect transistors, memories, and logic gates [4–8]. However, the ability to exploit valley polarizations has been somewhat limited until the recent emergence of 2D materials with honeycomb structures. In these hexagonal 2D materials, such as graphene and monolayer group-VI transition metal dichalcogenides (TMDs) (MoS_2, $MoSe_2$, WS_2, and WSe_2) [9–15], the electronic properties at the band edge are dominated by the two inequivalent valleys that occur at the K and K' points at the edges of the Brillouin zone. These valleys can be represented by a binary pseudospin that behaves like a spin-1/2 system; the electrons in the K valley can be labeled as valley-

pseudospin up, and the electrons in the K' valley can be labeled as valley-pseudospin down.

It is still a challenge in valleytronics to break the degeneracy between K and K' valley to produce valley polarization. For example, in a MoS_2 monolayer, the valley polarization could be triggered by circularly polarized light irradiation, whereas the luminescence lifetime is too short to practical application [9]. For materials such as $MnPSe_3$ [8] and VSe_2 [16], spontaneous valley polarization could be realized with the absence of time reversal symmetry. Especially for ferromagnetic materials, intrinsic valley polarization could be realized with a one-spin channel located at the valence band maximum (VBM) or conduct band minimum (CBM), where valley splitting emerges. After the proposal of anomalous valley Hall effect (AVHE) (i.e., the generation of charge Hall current under spontaneous valley polarization) in ferrovalley VSe_2, a lot of 2D intrinsic valley polarized ferromagnetic (FM) materials are proposed, such as $FeCl_2$ [17], Nb_3I_8 [18], $GdCl_2$ [19], and GdI_2 [20].

As to the mechanism of producing a nonequivalent valley at K and K', breaking the inversion symmetry is crucial. For instance, introduction of staggered AB sublattice potentials in honeycomb lattice could give rise to the quantum valley Hall effect (QVHE) [21–23] which is characterized by a valley Chern number $C_v = C_K - C_{K'}$. Although there are a lot of 2D materials exhibiting valley property, staggered AB sublattice potentials–induced valley polarization of $3d$ orbital in honeycomb lattice is rarely reported. Recently, a family of quantum anomalous Hall effect (QAHE) is reported in hexagonal kagome (HK) lattice A_2X_3 (A = V, Nb, and Ta; X =
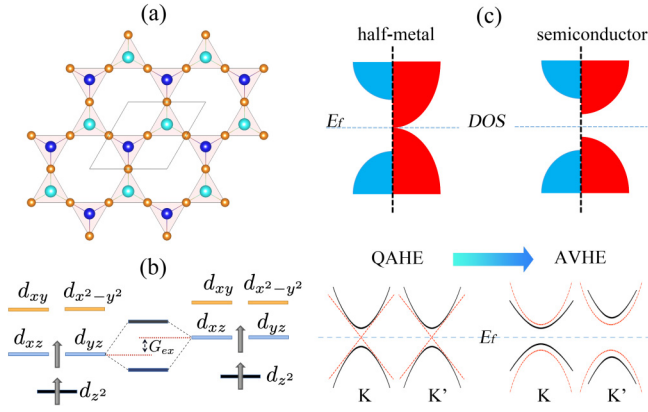
*turney0524@163.com
†wjnaf@163.com

FIG. 1. (a) Geometric structure of ABX_3 HK lattice, orange atoms connecting the semitransparent triangles represent X, and the atoms in the center of the semitransparent triangles represent two different metals A and B. (b) Schematic diagram of direct magnetic exchange mechanism for the FM coupling of ABX_3 HK lattice. (c) Phase transition from QAHE to AVHE by introduction of stagger potential represented by density of states (DOS) without SOC and bands, where the black line and red dash line are with and without SOC, respectively.

O, S, and benzene) [24–29], where the nontrivial topological properties are mainly contributed by d_{xz} and d_{yz} orbitals by the same two metals. Therefore, it is rational to infer that, by introduction of staggered AB sublattice potentials, the HK lattice may exhibit valley polarization.

The TB method is a powerful tool in condensed physics matter, and the electronic band structure can usually be well revealed by constructing a simple model with some rational parameters to provide a numerical solution or even an analytical solution, such as quantum spin Hall effect and optic lattice [30–32]. In this work, we constructed a four-band TB model in HK lattice and revealed the mechanism of valley polarization and the AVHE. We further derived a two-band kp model to reveal the connection between spin orbit coupling (SOC) strength and valley polarization. To certificate the mechanism in real 2D materials, we further performed density functional theory (DFT) calculations to study the electronic structure of NbV(C$_6$H$_4$)$_3$, TaNb(C$_6$H$_4$)$_3$, and NbTaO$_3$, which are suggested as valleytronic materials. Our DFT calculations reveal that they are intrinsic valley polarized and the value of valley polarization are consistent with our two-band kp model.

II. MECHANISM OF AVHE IN HK LATTICE ABX_3

A. Geometric structure and crystal field in ABX_3 monolayer

The geometric structure of ABX_3 HK lattice is shown in Fig. 1, where two different metals A and B and ligands X are denoted with cyan, blue, and orange atoms, respectively. The point group of the ABX_3 HK lattice is D_{3h}, and the C_3 rotation symmetric operation absent of inversion symmetry is crucial for valley character at K and K' in the reciprocal space.

As we discussed in our previous work [29], the number of valence electrons are crucial to stabilize the A_2X_3 HK lattice with similar orbital order. This mechanism also plays a key role in the ABX_3 HK lattice. As to metal atoms A and B, the

TABLE I. The connect vectors and the corresponding Slater-Koster parameters of NN hopping.

$\vec{r}_\delta$	$\langle\phi_{xz}\|H\|\phi_{xz}\rangle$	$\langle\phi_{xz}\|H\|\phi_{yz}\rangle$	$\langle\phi_{yz}\|H\|\phi_{yz}\rangle$
$(\frac{\sqrt{3}}{2}, \frac{1}{2})$	$\frac{1}{4}(3V_\pi + V_\delta)$	$-\frac{\sqrt{3}}{4}(V_\pi - V_\delta)$	$\frac{1}{4}(V_\pi + 3V_\delta)$
$(-\frac{\sqrt{3}}{2}, \frac{1}{2})$	$\frac{1}{4}(3V_\pi + V_\delta)$	$\frac{\sqrt{3}}{4}(V_\pi - V_\delta)$	$\frac{1}{4}(V_\pi + 3V_\delta)$
$(0, -1)$	V_δ	0	V_π

five d orbitals split into three groups: The lowest d_{z^2}, the middle (d_{xz}, d_{yz}), and the highest $(d_{xy}, d_{x^2-y^2})$ [see Fig. 1(b)]. We denote the energy difference of the (d_{xz}, d_{yz}) orbital between A and B as G_{ex}, which may play a key role in the enhancement of Curie temperature of the 2D lattice [33]. Compared with QAHE insulator A_2X_3 HK lattice, ABX_3 is characterized as a semiconductor induced by G_{ex}, which is also the band gap with absence of the SOC effect. The electronic band structure will transform from half-metal to half-semiconductor [see Fig. 1(c)].

B. Four-band effect tight-binding model

To reveal the AVHE of 2D ABX_3 HK lattice, we constructed a four-band effect tight-binding (TB) model with a basis of $(d_{A,xz}, d_{A,yz}, d_{B,xz}, d_{B,yz})^T$. As we discussed in our previous work [29] about 2D A_2X_3 HK lattice, the states are mainly from spin majority because of the crystal effect and the large spin exchange splitting. As a result, our TB model is constructed in Hilbert space of spin majority, and the Hamiltonian with absence of SOC reads

$$H_0 = \sum_i \varepsilon_i d_i^+ d_i + t_{i,j,\vec{\delta}} \sum_{\vec{r}_A, i} \left(d_{i,\vec{r}_A}^+ d_{j,\vec{r}_A+\vec{r}_\delta} + \text{H.c.} \right), \quad (1)$$

where ε_i is the on-site energy of different atoms, and $\vec{r}_\delta$ are vectors from A to its the nearest-neighbor (NN) B atoms. Here we discuss the Hamiltonian of only the NN coupling. The lattice vectors are chosen as $\vec{a} = \sqrt{3}(1,0)$; $\vec{b} = \sqrt{3}(1/2, \sqrt{3}/2)$, and the corresponding reciprocal lattice are $\vec{k}_a = 2\pi(1/\sqrt{3}, -1/3)$; $\vec{k}_b = 2\pi(0, 2/3)$. According to Slater-Koster rules, we listed the parameters of the hopping in Table I, in which V_π and V_δ are energies of π and δ bond of d orbitals, respectively.

With the derived Slater-Koster parameters, the Hamiltonian could be written as

$$H = \begin{pmatrix} m & 0 & \sum_\delta t_{(xz,xz;\vec{r}_\delta)}e^{i\vec{k}\cdot\vec{r}_\delta} & \sum_\delta t_{(xz,yz;\vec{r}_\delta)}e^{i\vec{k}\cdot\vec{r}_\delta} \\ 0 & m & \sum_\delta t_{(yz,xz;\vec{r}_\delta)}e^{i\vec{k}\cdot\vec{r}_\delta} & \sum_\delta t_{(yz,yz;\vec{r}_\delta)}e^{i\vec{k}\cdot\vec{r}_\delta} \\ & & -m & 0 \\ \text{H.c.} & 0 & & -m \end{pmatrix},$$
$$(2)$$

where $t_{i,j;\vec{r}_\delta} = \langle\phi_i|H|\phi_j\rangle$ and $m = \frac{1}{2}(\varepsilon_A - \varepsilon_B)$. Based on the Hamiltonian, the electronic band structure can be revealed with some rational parameters. The shape of the band is determined by the ratio of the three parameters $m : V_\pi : V_\delta$. We plotted the band structure with the ratio $m : V_\pi : V_\delta = 10 : 5 : 1$ and $m : V_\pi : V_\delta = 0 : 5 : 1$ [see Fig. 2(a)]. The result indicates that, when the on-site energy of A and B are equal,
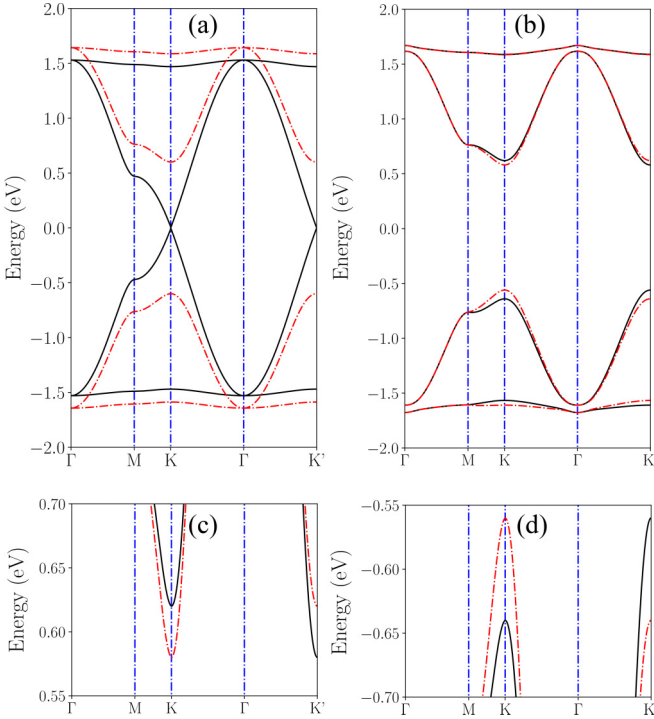
FIG. 2. (a) Band structures without SOC: The ones with and without G_{ex} are red dash and black line, respectively. (b)–(d) Band characters around the Fermi energy: The black and red dash lines represent the bands when spin directions are along $+z$ and $-z$, respectively.
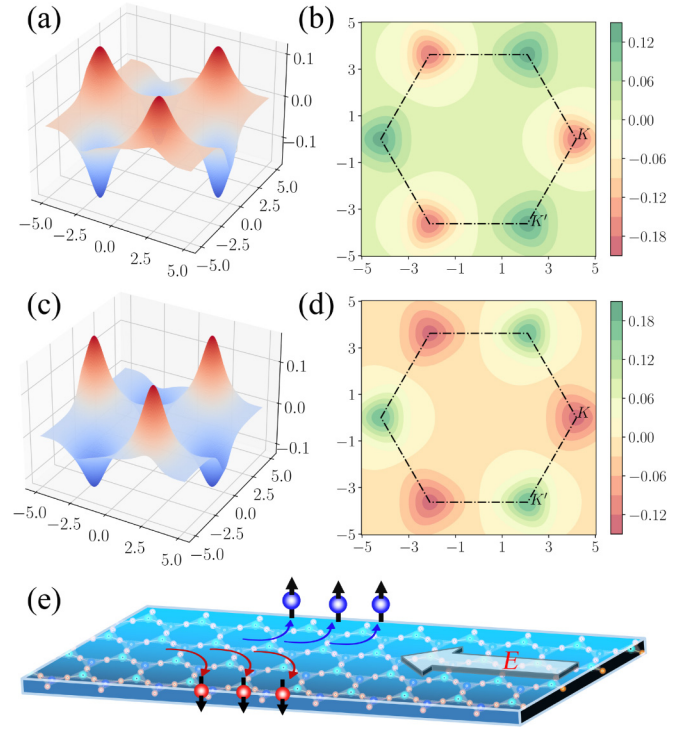

FIG. 3. Berry curvature of 2D ABX_3 HK lattice: Surface map (a) and contour map (b) when spin direction is along z; surface map (c) and contour map (d) when spin direction is along $-z$; (e) AVHE of electron at K' and K valley for spin direction along $+z$ and $-z$, respectively.

half-metallic Dirac states emerge, and the band will open a gap with the effect of on-site energy difference. Without the effect of SOC, the valley at K and K' are identical.

SOC is a crucial factor for valleytronics, based on the basis we mentioned above, and the Hamiltonian of SOC is written as

$$H_{\text{SOC}} = i\lambda_j \sum_{j=A,B} (d^+_{j,xz}d_{j,yz} - d^+_{j,yz}d_{j,xz}). \quad (3)$$

With the effect of SOC, the total Hamiltonian could be written as $H_{\text{tot},\uparrow} = H + H_{\text{SOC}}$. We further plotted the band with the parameter ratio $m : V_\pi : V_\delta : \lambda_A : \lambda_B = 10 : 5 : 1 : 1 : 2$ [see Figs. 2(b)–2(d)]. As shown in Fig. 2(b), the valley of K and K' is maintained because the SOC strength is small compared with that of hopping between different orbitals, and the degeneracy at the Γ point is broken with a gap. As shown in Figs. 2(c) and 2(d), intrinsic valley polarization occurs at both VBM and CBM.

As to intrinsic valley polarization 2D lattice, Berry curvature $\vec{\Omega}(\vec{k})$ is crucial for anomalous velocity of Bloch electron $\vec{v}_a \sim -\frac{e}{\hbar}\vec{E} \times \vec{\Omega}(\vec{k})$, where $\vec{E}$ is the external electric field. Based on the Kubo formula, Berry curvature of the 2D system can be written as

$$\Omega^z(\vec{k}) = -2Im \sum_m \sum_{m \neq n} f_n \frac{\langle n|v_x|m\rangle\langle m|v_y|n\rangle}{(E_m - E_n)^2}, \quad (4)$$

where f_n is the Fermi-Dirac distribution function, $|m\rangle(|n\rangle)$ is the wave function of the band index $m(n)$, and $v_x(v_y)$ is the velocity operator. The evaluated Berry curvature is shown in

Figs. 3(a) and 3(b), which reveal that the Berry curvature have different absolute values with opposite signs.

With the absence of time reversal symmetry, the spin-polarized carriers will transfer perpendicular to the in-plane electric field, thus realizing the AVHE. Spin-valley coupling is crucial for AVHE, and the direction of Berry curvature is spin dependent. Based on the basis we discussed above, we further calculated the band character and the Berry curvature when the spin direction is reversed.

To reverse the spin direction, we only need to reverse the Hamiltonian of the SOC part, and the corresponding total Hamiltonian can be written as $H_{\text{tot},\downarrow} = H - H_{\text{SOC}}$. The band structures are shown in Figs. 2(b)–2(d) (red dash lines), which indicate that the band character of K and K' will exchange with the reversion of spin direction. When the direction of spin flips, the valley polarization of both VBM and CBM will be flipped by spin, which is desirable for valleytronics.

As to Berry curvature, the signs do not change when the spin direction reverses, while the value of K and K' changes [see Figs. 3(c) and 3(d)]. As a result, AVHE emerges as shown in Fig. 3(e). When the spin direction is along $+z(-z)$, the electrons from the $K'(K)$ valley are accumulated on the left (right). The different Hall current gives rise to different in-plane Hall voltage perpendicular to the external in-plane electric field (E), therefore offering a possible avenue to realize data storage with valley polarization.

C. The derived two-band kp model and valley Chern number

As mentioned above, the sign of Berry curvature around K is opposite of that around K'. To reveal the origin of valley polarization, we further described the Hamiltonian H' with another base $(d_{A+}, d_{A-}, d_{B+}, d_{B-})^T$, where $d_{\pm} = \frac{\sqrt{2}}{2}(d_{xz} \pm d_{yz})$. The strength of π bond V_π is usually one order of magnitude larger than V_δ; here we simplified our model with an approximation of $V_\delta = 0$, which works well for the A_2X_3 HK lattice [24] and the Hamiltonian can be written as

$$
H' = \begin{pmatrix} -\lambda_A & 0 & \frac{V_\pi}{2}\sum_\delta e^{i\vec{k}\cdot\vec{r}_\delta} & \frac{V_\pi}{2}\sum_\delta e^{-i\theta_\delta}e^{i\vec{k}\cdot\vec{r}_\delta} \\ 0 & \lambda_A & \frac{V_\pi}{2}\sum_\delta e^{i\theta_\delta}e^{i\vec{k}\cdot\vec{r}_\delta} & \frac{V_\pi}{2}\sum_\delta e^{i\vec{k}\cdot\vec{r}_\delta} \\ & & -\lambda_B & 0 \\ \text{H.c.} & & 0 & \lambda_B \end{pmatrix},
$$

(5)

where $\theta_{\delta=1,2,3} = (\frac{\pi}{3}, \frac{5\pi}{3}, 3\pi)$.

We further expand the Hamiltonian H' to H_K at K,

$$
H_K = \begin{pmatrix} m - \lambda_A & 0 & \frac{3V_\pi}{4}(q_x - iq_y) & -\frac{3V_\pi}{2} \\ 0 & m + \lambda_A & \frac{3V_\pi}{4}(q_x + iq_y) & \frac{3V_\pi}{4}(q_x - iq_y) \\ & & -m - \lambda_B & 0 \\ \text{H.c.} & & 0 & -m + \lambda_B \end{pmatrix},
$$

(6)

and $H_{K'}$ at K',

$$
H_{K'} = \begin{pmatrix} m - \lambda_A & 0 & -\frac{3V_\pi}{4}(q_x + iq_y) & -\frac{3V_\pi}{4}(q_x - iq_y) \\ 0 & m + \lambda_A & -\frac{3V_\pi}{2} & -\frac{3V_\pi}{4}(q_x + iq_y) \\ & & -m - \lambda_B & 0 \\ \text{H.c.} & & 0 & -m + \lambda_B \end{pmatrix},
$$

(7)

where $(q_x, q_y) = \vec{k} - K(K')$ at $K(K')$ point. For H_K, eigenvalues of the middle two bands are $m + \lambda_A$ and $-(m + \lambda_B)$, and the corresponding eigenvectors are $(0, 0, 1, 0)^T$ and $(0, 1, 0, 0)^T$, respectively. As a result, we could simplify the four-band Hamiltonian to a effective two-band kp Hamiltonian H_K^{eff}:

$$
H_K^{\text{eff}} = \begin{pmatrix} m + \lambda_A & \frac{3V_\pi}{4}(q_x + iq_y) \\ \frac{3V_\pi}{4}(q_x - iq_y) & -m - \lambda_B \end{pmatrix}.
$$

(8)

Similarly, eigenvalues of the middle two bands for K' point are $m - \lambda_A$ and $-(m - \lambda_B)$, and the corresponding eigenvectors are $(1, 0, 0, 0)^T$ and $(0, 0, 0, 1)^T$, respectively. The simplified effective two-band kp Hamiltonian $H_{K'}^{\text{eff}}$ can be written as

$$
H_{K'}^{\text{eff}} = \begin{pmatrix} m - \lambda_A & -\frac{3V_\pi}{4}(q_x - iq_y) \\ -\frac{3V_\pi}{4}(q_x + iq_y) & \lambda_B - m \end{pmatrix}.
$$

(9)

The result indicates that the valley splitting of VBM and CBM is $\triangle_v = 2\lambda_B$ and $\triangle_c = 2\lambda_A$, respectively. The difference in the band gap between K and K' $\triangle_G = 2(\lambda_A + \lambda_B)$. With the index of valley τ, the total two-band kp Hamiltonian can be written as $H^{\text{eff}} = \tau\frac{3V_\pi}{4}q_x\sigma_x - \frac{3V_\pi}{4}q_y\sigma_y + (m +$

$\tau\frac{\lambda_A+\lambda_B}{2})\sigma_z + \tau\frac{\lambda_A-\lambda_B}{2}\sigma_0$, where $\tau = 1$ for K valley and $\tau = -1$ for K' valley.

To characterize the valley Chern number, we further calculated the Chern number of both K and K' with the simplified kp Hamiltonian. As to a two-band general model $H = \sum_i d_i(\vec{k})\sigma_i = \sum_{i,j} k_i A_{ij}\sigma_j + M\sigma_z + n\sigma_0$, the Berry curvature is expressed as $\Omega(\vec{k}) = \frac{M}{2d^3}\det(A)$, where $d = \sqrt{d_1^2 + d_2^2 + d_3^2}$. The corresponding Chern number $C_k = \frac{1}{2}\text{sign}(M)\text{sign}(\det A)$. As to H_K^{eff}, $A_{11} = \frac{3V_\pi}{4}$, $A_{22} = -\frac{3V_\pi}{4}$, $A_{12} = A_{21} = 0$, and $M = m + \frac{\lambda_A+\lambda_B}{2}$. As a result, the Chern number at K point is $-1/2$. As to $H_{K'}^{\text{eff}}$, $A_{11} = -\frac{3V_\pi}{4}$, $A_{22} = -\frac{3V_\pi}{4}$, $A_{12} = A_{21} = 0$, and $M = m - \frac{\lambda_A+\lambda_B}{2}$. So the Chern number at K' is $1/2$, and the valley Chern number $C_v = C_K - C_{K'} = -1$.

In summary, the degenerate valley at K and K' is induced by a C_3 rotation point symmetry. To lift the degeneracy of the valleys, inversion and time reversal symmetry should be broken and SOC is also crucial. Our four-TB model and the derived two-band kp model reveal that, in ferromagnetic HK lattice, the two orbitals d_{xz} and d_{yz} of the spin-up channel in two different sites of A and B give rise to valley character and the stagger potential between A and B gives rise to a semiconductor property. When SOC is considered, the effective two-band Hamiltonian suggests that the on-site energy is different between K and K' by the effect of SOC and stagger potential, and therefore AVHE emerges.

III. MATERIALS REALIZATION

Here we choose 2D HK triphenyl-metal lattice TaNb$(C_6H_4)_3$ and NbV$(C_6H_4)_3$ to realize the mechanism of AVHE. Both of them are in the formula of ABX_3, where X is organic ligand of C_6H_4 and A and B are (Nb, V) and (Ta, Nb), respectively. The geometric structures are first optimized by our DFT calculations, which we also performed to verify the stability and to investigate the electronic structures of the 2D HK triphenyl-metal lattice.

A. Computational details of first-principles method

DFT calculations of geometric structures, electronic band structures, and thermal property were carried out using the Vienna *ab initio* simulation package (VASP) with the projector augmented wave (PAW) method [34,35]. The exchange-correlation potential of the Perdew–Burke–Ernzerhof (PBE) functional was adopted [36]. We take a large plane-wave cutoff of 600 eV. The convergence criterion energy and Hellman-Feynman forces was set to be 10^{-6} eV and 10^{-3} eV/Å, respectively. For Brillouin-zone integrations, Γ-centered $15 \times 15 \times 1$ Monkhorst-Pack k-point meshes are used. In the ab initio molecular dynamics (AIMD) simulations, the particle-volume-temperature ensemble was adopted. The time step was set to be 1.0 fs and the temperature was controlled by the Nosé-Hoover method [37].

B. Geometric structures and stability

The optimized geometric structures of the two materials are shown in Fig. 4. There are two transition metal atoms and
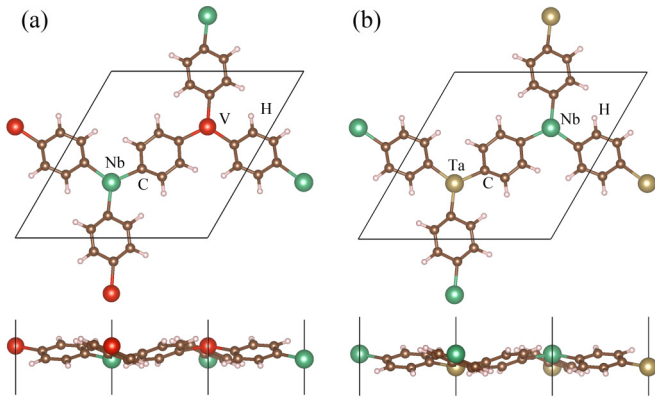
FIG. 4. The geometric structures of $NbV(C_6H_4)_3$ (a) and $TaNb(C_6H_4)_3$ (b).

three benzene rings in each unit cell. The lattice is slightly buckled and the three benzene rotates along the same direction relative to the bridge of metal-benzene ring-metal bonds, which gives rise to a C_3 point group symmetry.

To investigate the thermal stability of $NbV(C_6H_4)_3$ and $TaNb(C_6H_4)_3$, we performed AIMD calculations at 300 K with a supercell of $2 \times 2 \times 1$ for both structures. The structure at the end of the AIMD calculations and the bond-length variation during the AIMD steps are shown in Fig. 5. The results suggest that the bonds maintained well in the whole range of AIMD calculations, which pronounces thermal stability of $NbV(C_6H_4)_3$ and $TaNb(C_6H_4)_3$ lattice.

C. Magnetic properties and electronic band structures

The ground state of both $NbV(C_6H_4)_3$ and $TaNb(C_6H_4)_3$ is FM with a magnetic moment of $2\,\mu_B$ for each metal atom, and the spin direction is perpendicular to the basal plane. The magnetic anisotropic energy (MAE) for $NbV(C_6H_4)_3$ and $TaNb(C_6H_4)_3$ is 0.59 and 9.21 meV, respec-
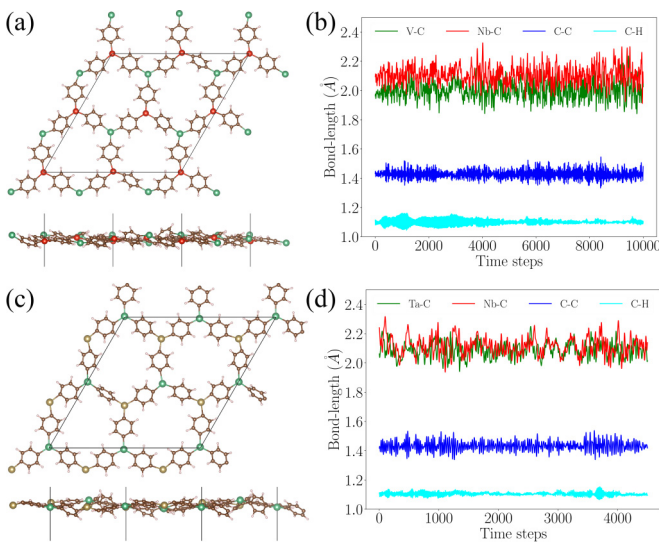
FIG. 5. The geometric structures at the end of the AIMD calculations of $NbV(C_6H_4)_3$ (a) and $TaNb(C_6H_4)_3$ (c); (b) and (d) are the bond variation during the whole AIMD time steps for $NbV(C_6H_4)_3$ and $TaNb(C_6H_4)_3$, respectively.
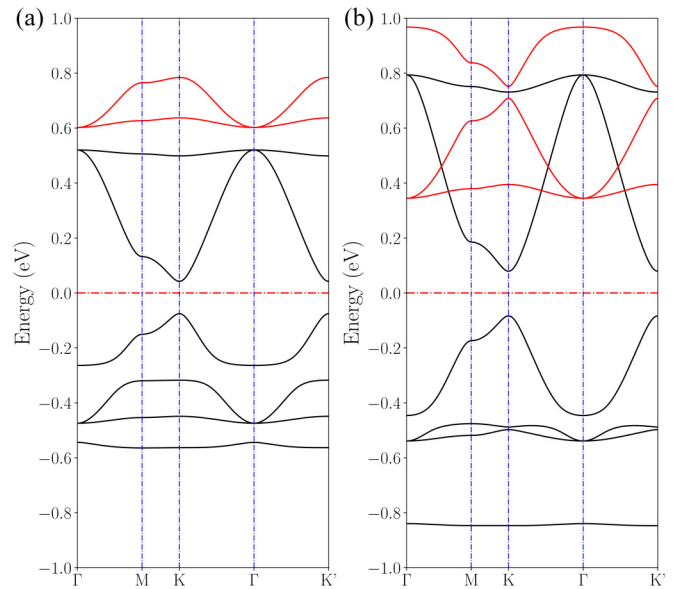
FIG. 6. The electronic band structures without SOC of $NbV(C_6H_4)_3$ (a) and $TaNb(C_6H_4)_3$ (b). The black and red line are spin up and spin down, respectively.

tively. We also compared the energy difference of FM and ferrimagnetic (FIM) states, which is 0.476 and 0.409 eV for $NbV(C_6H_4)_3$ and $TaNb(C_6H_4)_3$, respectively. The exchange coupling strength is weaker than that of $V_2(C_6H_4)_3$ (0.504 eV) and stronger than that of $Nb_2(C_6H_4)_3$ (0.298 eV) [29]. It suggests that the crystal effect is also crucial for the exchange coupling besides the virtual exchange gap [33].

The electronic band structure of the two materials without SOC is shown in Fig. 6, in which the band gap is from the on-site-energy difference between the two atoms in the ABX_3 lattice compared with gapless A_2X_3 lattice. As to the planar structure, in which the benzene rings are parallel to the basal plane without rotation, the band structure could be well described by our four-band model (see Figs. S1 [38], 7, and
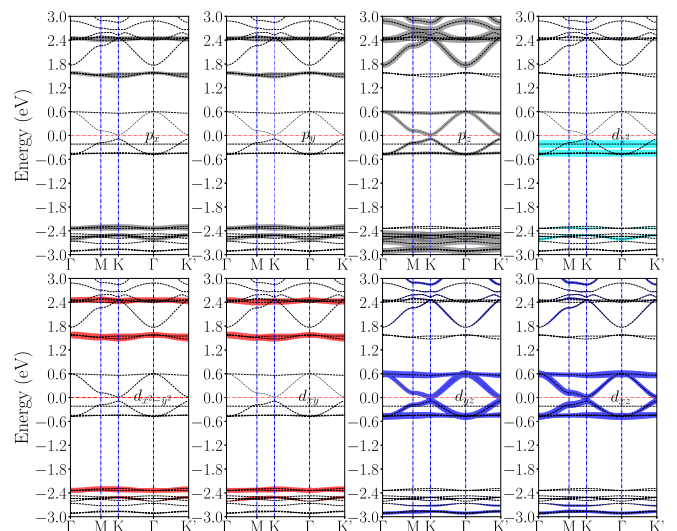

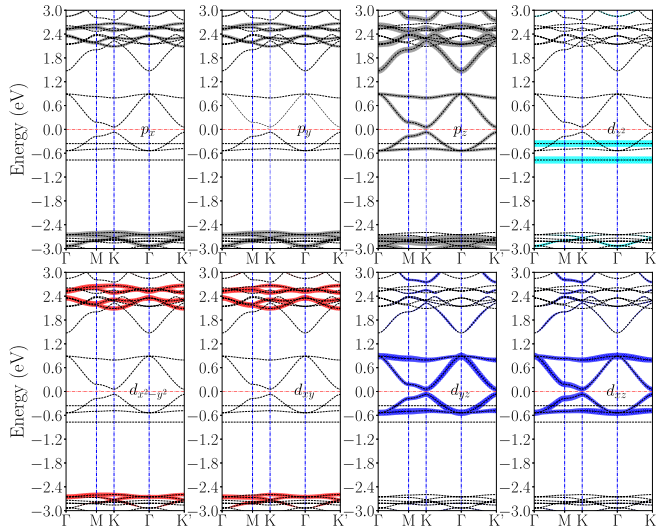FIG. 7. The electronic band projection of spin majority for planar $NbV(C_6H_4)_3$.

FIG. 8. The electronic band projection of spin majority for planar TaNb(C$_6$H$_4$)$_3$.

8). As to the low buckled structures, as shown in Figs. S2 and S3 [38], the VBM and CBM are mainly from the d_{xz} and d_{yz} orbital, and there is some hybridization between the d_{z^2} and p_z orbital around the Fermi energy level. Nevertheless, the valley splitting around K and K' is irrelevant to the hybridization, which could not give rise to band splitting around K or K'. As a result, our derived two-band kp model still works well.

We further plotted the band structure with SOC effect around K and K' point (see Fig. 9). As discussed above, with the effect of SOC, both VBM and CBM, which are mainly from d_{xz} and d_{yz} around K and K', will split. In addition, the band splitting at VBM and CBM will increase the valley splitting. We listed the values of band splitting in Table II, including band splitting of CBM ($\triangle_C$) and VBM ($\triangle_V$), valley splitting ($\triangle_G$), and the band gap of K (G_K) and K' ($G_{K'}$). The results are consistent with that of our two-band kp model, the valley polarization of NbV(C$_6$H$_4$)$_3$ is comparable with that of GdCl$_2$ (42.3 meV) [19], and the valley polarization of TaNb(C$_6$H$_4$)$_3$ is even larger than that of Nb$_3$I$_8$ (107 meV) [18].
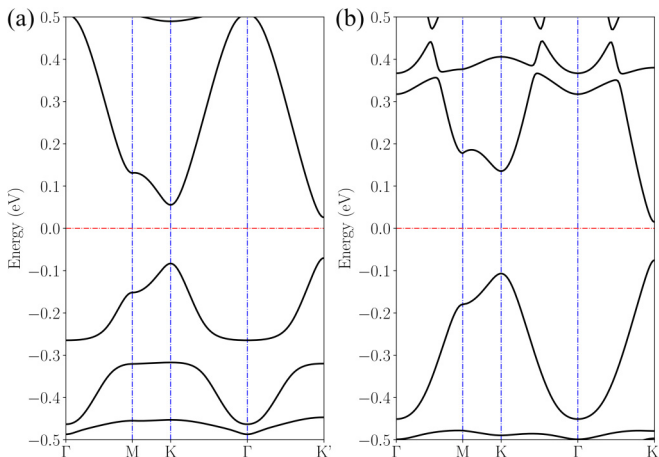
FIG. 9. The electronic band structures with SOC: (a) NbV(C$_6$H$_4$)$_3$ and (b) TaNb(C$_6$H$_4$)$_3$.

TABLE II. Band gap and valley polarization of NbV(C$_6$H$_4$)$_3$ and TaNb(C$_6$H$_4$)$_3$ (in units of meV).

	G_K	$G_{K'}$	$\triangle_C$	$\triangle_V$	$\triangle_G$
NbV(C$_6$H$_4$)$_3$	138.67	95.95	29.67	13.04	42.72
TaNb(C$_6$H$_4$)$_3$	242.22	90.00	120.48	31.74	152.23

To investigate the AVHE, we further calculated the Berry curvature in the Brillouin zone of both NbV(C$_6$H$_4$)$_3$ and TaNb(C$_6$H$_4$)$_3$ (see Fig. 10) [41]. The results show that the maximum and the minimum of the Berry curvature are located at the K' and K point, respectively, and it is also consistent with our kp model.

Besides, we also tested the 2D HK metal oxide TaNbO$_3$ monolayer, whose stability is verified by our phonon and AIMD calculation (see Fig. S4 [38]). The band structure (see Fig. S5 [38]) suggests that valley polarization can also be induced in the TaNbO$_3$ monolayer. Based on the results we discussed above, we may expect that this mechanism could be employed to other 2D HK lattice A_2X_3 to introduce valley polarization by substitution of one of the two metals A with a different metal B.

IV. CONCLUSION

In this work, we proposed valley polarization and the AVHE mechanism in ABX_3 HK lattice by constructing a four-band TB model in the basis of $(d_{A,xz}, d_{A,yz}, d_{B,xz}, d_{B,yz})^T$. Our TB model reveals that it will exhibit a phase transition from QAHE to AVHE by substituting metal A in A_2X_3 with a proper different metal B. The substituting breaks the inversion symmetry of the HK lattice, whereas the point group symmetry of C_3 is retained. As a result, in the electronic band structures around the Fermi energy level, it is mainly from d_{xz} and d_{yz} orbitals induced by the corresponding crystal field of the C_3 point group. We further reveal that the derived two-band kp model could well describe the wave vector and eigenvalues of VBM and CBM, and the valley polarization could be analytically solved. SOC and stagger potential in the basis of d_{xz} and d_{yz} of two sites in HK lattice give rise to the AVHE.
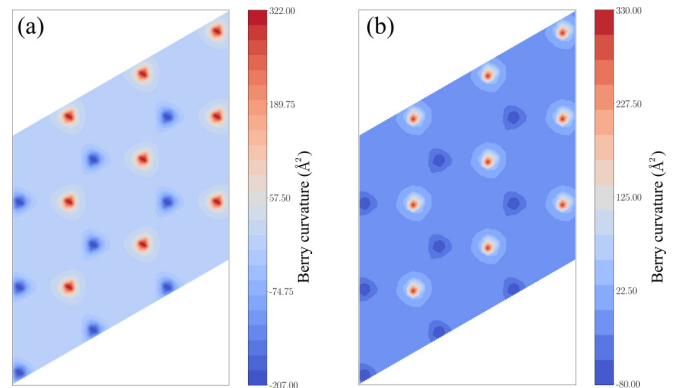

FIG. 10. Berry curvature of NbV(C$_6$H$_4$)$_3$ (a) and TaNb(C$_6$H$_4$)$_3$ (b).

Based on the mechanism we proposed, we successfully realized intrinsic valley polarization and AVHE in 2D HK metal organic lattice $NbV(C_6H_4)_3$ and $TaNb(C_6H_4)_3$. The results in the materials are consistent with our proposal in the model. They exhibit a ground state of FM and the spin direction is perpendicular to the plane, which is crucial for long-range order of magnetism. The energy of exchange coupling and magnetic anisotropic energy is large and comparable to that of room temperature FM HK lattice $Nb_2(C_6H_4)_3$ and $Ta_2(C_6H_4)_3$. The valley polarizations for $NbV(C_6H_4)_3$ and $TaNb(C_6H_4)_3$ are 42.72 and 152.23 meV, respectively, which are large enough and favorable for application in valleytronics.

[1] J. R. Schaibley, H. Yu, G. Clark, P. Rivera, J. S. Ross, K. L. Seyler, W. Yao, and X. Xu, Valleytronics in 2D materials, Nat. Rev. Mater. **1**, 16055 (2016).

[2] Y. Liu, Y. Gao, S. Zhang, J. He, J. Yu, and Z. Liu, Valleytronics in transition metal dichalcogenides materials, Nano Res. **12**, 2695 (2019).

[3] K. F. Mak, D. Xiao, and J. Shan, Light–valley interactions in 2D semiconductors, Nat. Photonics **12**, 451 (2018).

[4] N.-Y. Lue, Y. C. Chen, and G. Y. Wu, Valley-based field-effect transistors in graphene, Phys. Rev. B **87**, 039904(E) (2013).

[5] A. Rycerz, J. Tworzydlo, and C. W. J. Beenakker, Valley filter and valley valve in graphene, Nat. Phys. **3**, 172 (2007).

[6] Q. Liu, X. Zhang, and A. Zunger, Intrinsic Circular Polarization in Centrosymmetric Stacks of Transition-Metal Dichalcogenide Compounds, Phys. Rev. Lett. **114**, 087402 (2015).

[7] F. Zhang, A. H. MacDonald, and E. J. Mele, Valley Chern numbers and boundary modes in gapped bilayer graphene, Proc. Natl. Acad. Sci. USA **110**, 10546 (2013).

[8] X. Li, T. Cao, Q. Niu, J. Shi, and J. Feng, Coupling the valley degree of freedom to antiferromagnetic order, Proc. Natl. Acad. Sci. USA **110**, 3738 (2013).

[9] K. F. Mak, K. L. Mcgill, J. Park, and P. L. Mceuen, The valley Hall effect in MoS_2 transistors, Science **344**, 1489 (2014).

[10] X. Xu, W. Yao, D. Xiao, and T. F. Heinz, Spin and pseudospins in layered transition metal dichalcogenides, Nat. Phys. **10**, 343 (2014).

[11] A. M. Jones, H. Yu, N. J. Ghimire, S. Wu, G. Aivazian, J. S. Ross, B. Zhao, J. Yan, D. G. Mandrus, D. Xiao, W. Yao, and X. Xu, Optical generation of excitonic valley coherence in monolayer WSe_2, Nat. Nanotechnol. **8**, 634 (2013).

[12] D. Xiao, G. B. Liu, W. Feng, X. Xu, and W. Yao, Coupled Spin and Valley Physics in Monolayers of MoS_2 and Other Group-VI Dichalcogenides, Phys. Rev. Lett. **108**, 196802 (2012).

[13] A. Kuc and T. Heine, The electronic structure calculations of two-dimensional transition-metal dichalcogenides in the presence of external electric and magnetic fields, Chem. Soc. Rev. **44**, 2603 (2015).

[14] J. Lee, K. F. Mak, and J. Shan, Electrical control of the valley Hall effect in bilayer MoS_2 transistors, Nat. Nanotechnol. **11**, 421 (2016).

[15] Z. Wu, B. T. Zhou, X. Cai, P. Cheung, G.-B. Liu, M. Huang, J. Lin, T. Han, L. An, Y. Wang, S. Xu, G. Long, C. Cheng, K. T. Law, F. Zhang, and N. Wang, Intrinsic valley Hall transport in atomically thin MoS_2, Nat. Commun. **10**, 611 (2019).

[16] W.-Y. Tong, S.-J. Gong, X. Wan, and C.-G. Duan, Concepts of ferrovalley material and anomalous valley Hall effect, Nat. Commun. **7**, 13612 (2016).

[17] P. Zhao, Y. Dai, H. Wang, B. Huang, and Y. Ma, Intrinsic valley polarization and anomalous valley Hall effect in single-layer 2H-FeCl₂, Chem. Phys. Mater. **1**, 56 (2022).

[18] R. Peng, Y. Ma, X. Xu, Z. He, B. Huang, and Y. Dai, Intrinsic anomalous valley Hall effect in single-layer Nb_3I_8, Phys. Rev. B **102**, 035412 (2020).

[19] S.-D. Guo, J.-X. Zhu, W.-Q. Mu, and B.-G. Liu, Possible way to achieve anomalous valley Hall effect by piezoelectric effect in a $GdCl_2$ monolayer, Phys. Rev. B **104**, 224428 (2021).

[20] H.-X. Cheng, J. Zhou, W. Ji, Y.-N. Zhang, and Y.-P. Feng, Two-dimensional intrinsic ferrovalley GdI_2 with large valley polarization, Phys. Rev. B **103**, 125121 (2021).

[21] D. Xiao, W. Yao, and Q. Niu, Valley-Contrasting Physics in Graphene: Magnetic Moment and Topological Transport, Phys. Rev. Lett. **99**, 236809 (2007).

[22] W. Yao, D. Xiao, and Q. Niu, Valley-dependent optoelectronics from inversion symmetry breaking, Phys. Rev. B **77**, 235406 (2008).

[23] W. Yao, S. A. Yang, and Q. Niu, Edge States in Graphene: From Gapped Flat-Band to Gapless Chiral Modes, Phys. Rev. Lett. **102**, 096801 (2009).

[24] H. P. Wang, W. Luo, and H. J. Xiang, Prediction of high-temperature quantum anomalous Hall effect in two-dimensional transition-metal oxides, Phys. Rev. B **95**, 125430 (2017).

[25] S.-J. Zhang, C.-W. Zhang, S.-F. Zhang, W.-X. Ji, P. Li, P.-J. Wang, S.-S. Li, and S.-S. Yan, Intrinsic Dirac half-metal and quantum anomalous Hall phase in a hexagonal metal-oxide lattice, Phys. Rev. B **96**, 205433 (2017).

[26] L. Zhang, C.-W. Zhang, S.-F. Zhang, W.-X. Ji, P. Li, and P.-J. Wang, Two-dimensional honeycomb-kagome Ta_2S_3: A promising single-spin Dirac fermion and quantum anomalous Hall insulator with half-metallic edge states, Nanoscale **11**, 5666 (2019).

[27] Z. F. Wang, Z. Liu, and F. Liu, Quantum Anomalous Hall Effect in 2D Organic Topological Insulators, Phys. Rev. Lett. **110**, 196801 (2013).

[28] N. Su, W. Jiang, Z. Wang, and F. Liu, Prediction of large gap flat Chern band in a two-dimensional metal-organic framework, Appl. Phys. Lett. **112**, 033301 (2018).

[29] B. Zhang, F. Deng, X. Chen, X. Lv, and J. Wang, Quantum anomalous Hall effect in M_2X_3 honeycomb Kagome lattice, J. Phys.: Condens. Matter **34**, 475702 (2022).

[30] C.-C. Liu, S. Guan, Z. Song, S. A. Yang, J. Yang, and Y. Yao, Low-energy effective Hamiltonian for giant-gap quantum spin Hall insulators in honeycomb X-hydride/halide

($X =$ Ni-Bi) monolayers, Phys. Rev. B **90**, 085431 (2014).

[31] C.-C. Liu, H. Jiang, and Y. Yao, Low-energy effective Hamiltonian involving spin-orbit coupling in silicene and two-dimensional germanium and tin, Phys. Rev. B **84**, 195430 (2011).

[32] C. Wu and S. D. Sarma, $p_{x,y}$-orbital counterpart of graphene: Cold atoms in the honeycomb optical lattice, Phys. Rev. B **77**, 235107 (2008).

[33] C. Huang, J. Feng, F. Wu, D. Ahmed, B. Huang, H. Xiang, K. Deng, and E. Kan, Toward Intrinsic room-temperature ferromagnetism in two-dimensional semiconductors, J. Am. Chem. Soc. **140**, 11519 (2018).

[34] G. Kresse and J. Furthmüller, Efficiency of ab-initio total energy calculations for metals and semiconductors using a plane-wave basis set, Comput. Mater. Sci. **6**, 15 (1996).

[35] G. Kresse and J. Furthmüller, Efficient iterative schemes for ab initio total-energy calculations using a plane-wave basis set, Phys. Rev. B **54**, 11169 (1996).

[36] J. P. Perdew, K. Burke, and M. Ernzerhof, Generalized Gradient Approximation Made Simple, Phys. Rev. Lett. **77**, 3865 (1996).

[37] G. J. Martyna, M. L. Klein, and M. Tuckerman, Nosé-Hoover chains: The canonical ensemble via continuous dynamics, J. Chem. Phys. **97**, 2635 (1992).

[38] See Supplemental Material at http://link.aps.org/supplemental/10.1103/PhysRevB.108.045146 for the band structures of $NbV(C_6H_4)_3$, $NbV(C_6H_4)_3$, and $TaNbO_3$, whose phonon band structure and AIMD results are also provided. The Supplemental Material also contains Refs. [39,40].

[39] A. Togo and I. Tanaka, First principles phonon calculations in materials science, Scr. Mater. **108**, 1 (2015).

[40] S. Baroni, S. D. Gironcoli, A. D. Corso, and P. Giannozzi, Phonons and related crystal properties from density-functional perturbation theory, Rev. Mod. Phys. **73**, 515 (2001).

[41] S.-W. Kim, H.-J. Kim, S. Cheon, and T.-H. Kim, Circular Dichroism of Emergent Chiral Stacking Orders in Quasi-One-Dimensional Charge Density Waves, Phys. Rev. Lett. **128**, 046401 (2022).